ACS Photonics

Letter

Cite This: ACS Photonics 2018, 5, 1196−1201

Guided Modes of Anisotropic van der Waals Materials Investigated by near-Field Scanning Optical Microscopy

Daniel Wintz,[†,‡] Kundan Chaudhary,[†,‡] Ke Wang,[§] Luis A. Jauregui,[§] Antonio Ambrosio,[∥] Michele Tamagnone,[†] Alexander Y. Zhu,[†] Robert C. Devlin,[†] Jesse D. Crossno,[†] Kateryna Pistunova,[§] Kenji Watanabe,[⊥] Takashi Taniguchi,[⊥] Philip Kim,[§] and Federico Capasso*[,†]

[†]Harvard John A. Paulson School of Engineering and Applied Sciences, [§]Department of Physics, and [∥]Center for Nanoscale Systems, Harvard University, Cambridge, Massachusetts 02138, United States

[⊥]National Institute for Materials Science, Namiki 1-1, Tsukuba, Ibaraki 305-0044, Japan

Supporting Information

ABSTRACT: Guided modes in nanometer thick anisotropic van der Waals materials are experimentally investigated and their refractive indices in visible wavelengths are extracted. Our method involves near-field scanning optical microscopy of waveguide (transverse electric) and surface plasmon polariton (transverse magnetic) modes in h-BN/SiO_2/Si and Ag/h-BN stacks, respectively. We determine the dispersion of these modes and use this relationship to extract anisotropic refractive indices of h-BN flakes. In the wavelength interval 550−700 nm, the in-plane and out-of-plane refractive indices are in the range 1.98−2.12 and 1.45−2.12, respectively. Our approach of using near-field scanning optical microscopy allows for the direct study of the interaction between light and two-dimensional van der Waals materials and heterostructures.

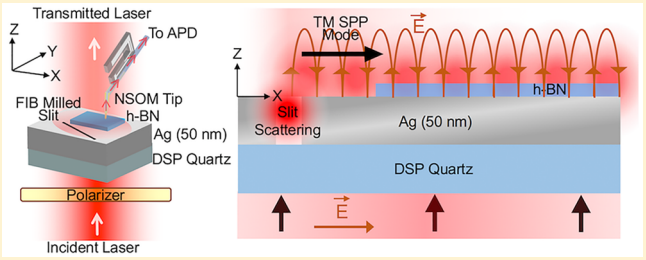

KEYWORDS: *2D materials, hexagonal boron nitride, near-field scanning optical microscopy, optical constants*

Two-dimensional (2D) materials have recently garnered significant interest due to their high electrical mobility, atomic-level flatness, and large exciton binding energies that enable versatile nanophotonics and optoelectronics applications.[1−23] However, the understanding of the interaction of visible light surface plasmon polaritons with 2D materials and more complex van der Waals (vdW) heterostructures[5−7] is still in its infancy.[9,23] In this work, we report a near-field scanning optical microscopy (NSOM)[25−28] study of highly crystalline hexagonal boron nitride (h-BN)[21] mechanically exfoliated flakes at visible wavelengths, demonstrating the direct observation of (i) transverse electric (TE) waveguide modes supported by h-BN on SiO_2 and (ii) the interaction of transverse magnetic (TM) surface plasmon polariton (SPP) modes supported by silver (Ag) with a thin h-BN flake. From NSOM scans, we estimate the intrinsically anisotropic optical dielectric constants ($n_x = n_y \neq n_z$) of h-BN, which is an arduous task by conventional methods such as ellipsometry.[24] Our technique can be extended to other vdW solids and heterostructures, where we anticipate the study of guided modes coupled to 2D materials to be a useful tool in exploring rich physics of surface polaritons,[9−14] plexcitons (SPPs-excitons),[29] gate-tunable,[17,30,31] layer number dependent optical properties,[13] in-plane anisotropy,[15,23] and selective circular dichroism.[18,19]

RESULTS AND DISCUSSION

For our experiments, we fabricate waveguiding h-BN structures patterned using electron beam lithography (EBL, see Methods) on two different substrates. In the first case (Figure 1a), a 65 nm thin flake of h-BN is placed on top of a silicon (Si) substrate with 285 nm of thermal oxide (SiO_2). Because the refractive index of bulk h-BN is larger than the one of SiO_2, asymmetric TE dielectric slab waveguide modes supported by the h-BN are to be expected.

Any guided mode is by definition evanescent, which means it cannot be observed with common optical microscopes that detect only far fields. To probe the near-fields on the samples, we use an NSOM in collection mode (Nanonics Imaging Ltd.), which utilizes a scanning metallized tapered fiber optic tip with a subwavelength aperture (effective diameter ∼ 50 nm).[25−28] An avalanche photodetector (APD) is connected at the other side of the fiber, such that the measured signal is proportional to the local optical intensity at the tip. A supercontinuum laser (NKT Photonics supercontinuum laser) is used to illuminate the sample from above with a filter (NKT Select) selecting a single wavelength with a 10 nm bandwidth in the spectral range from 550 to 700 nm. The impinging Gaussian beam, which can be approximated locally as a plane wave, can excite guided modes in the h-BN structure due to the scattering at the sample edges (Figure 1b). In the near-field region of h-BN, the optical electric field is the superposition of the impinging beam and the guided TE mode, creating interference fringes in the near-field

Received: December 11, 2017
Published: January 27, 2018

DOI: 10.1021/acsphotonics.7b01518
ACS Photonics 2018, 5, 1196−1201

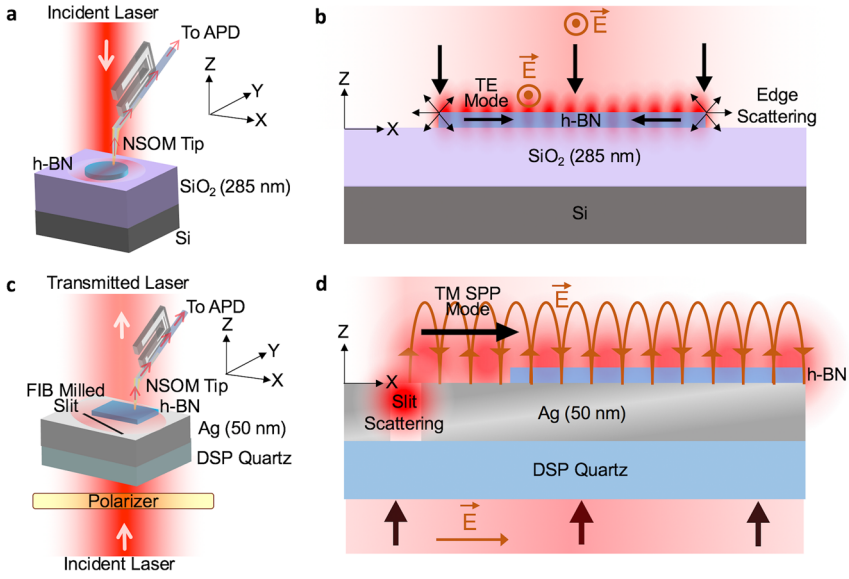

Figure 1. NSOM observation of guided modes in h-BN. (a) TE modes observation with NSOM setup in collection mode and top-side laser illumination. The sample is a 65 nm thick h-BN flake on Si + 285 nm SiO_2 substrate. (b) Formation of fringes due to the interference of TE guided mode and the illuminating beam. The edges of the sample scatter the incident beam which subsequently launches the TE waveguide modes. The fringes are not due to the stationary waves in the flake, but rather due to the interference of the guided mode with the Gaussian beam focused on the sample. See Supporting Information for more details. (c) TM SPP modes observation with NSOM setup in collection mode and back-side laser illumination. The sample is a 10 nm thick h-BN flake on 50 nm Ag on a double side polished (DSP) quartz substrate. (d) Formation of fringes due to interference of TM SPP guided mode and the beam transmitted through the Ag layer. SPPs are launched by a slit created in the Ag layer by focused ion beam (FIB) milling, and subsequently propagate in the region of the sample covered with h-BN. In both geometries (a, b) and (c, d), the impinging and guided modes have the same polarization (electric field). Subsequently, the fringes arise from interference of excited guided modes and incident beam and are directly observed by the NSOM probe as a variation of the local optical intensity.

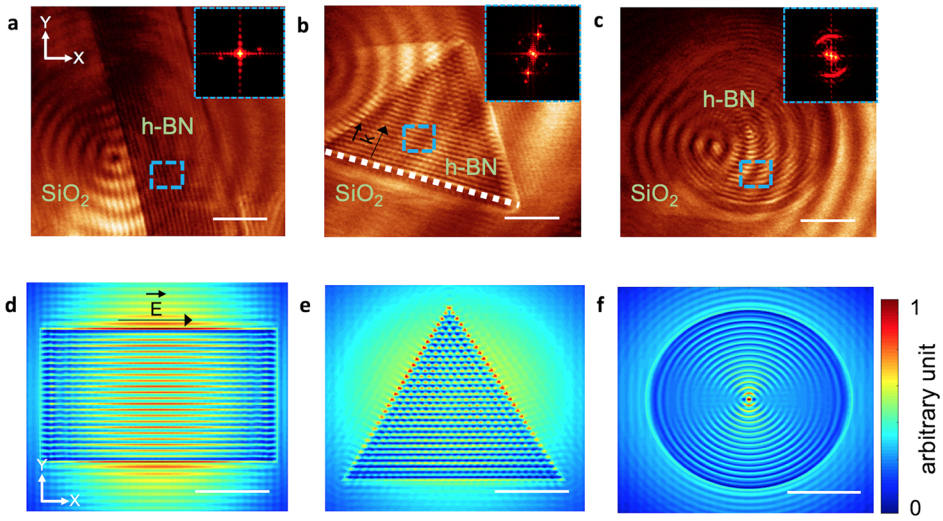

Figure 2. NSOM observation of TE waveguide modes in h-BN. (a–c) Measurement of the optical intensity of interference fringes for $\lambda = 650$ nm in patterned flakes (rectangle, triangle, and circle, respectively). The larger fringes with greater interfringe spacing are the result of the focusing of the Gaussian beam (see Supporting Information). Short period fringes (inside the h-BN region) correspond to high wavevector guided modes. Insets show the fast Fourier transform (FFT) of the corresponding region in the blue dashed rectangle. (d–f) Finite difference time domain (FDTD) simulation of the selected h-BN sample geometries, highlighting the guided wave pattern, with fringes spaced by $\lambda = \lambda_0/n_{eff}$, where λ_0 is the free space wavelength and n_{eff} is the effective index of the waveguide mode. The excitation beam is polarized along x-axis. The hot spots on the triangle in (b) and (e) are due to the intersections of fringes originating from all the edges (see Supporting Information for mathematical description). The fringes parallel to the edge in (b), highlighted by a dashed white line, are dominant with respect to fringes parallel to other edges. This is due to the fact that the incident beam is polarized and therefore the intensity of the fringes depends on their orientation with respect to the polarization of the incident beam. In particular, as described in Supporting Information, the intensity of each guided mode and its fringes is maximized when the incident polarization is parallel to the edge. Scale bars in (a)–(f) are 5 μm.

which can be imaged by the NSOM tip.[32,33] Here, the Gaussian beam at a normal incidence allows for isotropic interference fringes, unlike anisotropic fringes observed for illumination at an angle.[34]

For the second case (Figure 1c), the flakes are placed on a 50 nm thin Ag film on DSP quartz, and SPPs are launched using a 200 nm wide slit (milled with FIB) illuminated from the back-side, as described in our previous work.[32] Similar to the

DOI: 10.1021/acsphotonics.7b01518
ACS Photonics 2018, 5, 1196–1201

first case, the NSOM can image the SPPs and fringes are visible due to the interference of the SPPs and the transmitted beam (Figure 1d). The h-BN flake is placed in the path of the SPP, and the resulting SPP mode, modified by the presence of the h-BN, can be studied with NSOM scans of the near-field of the sample.

Figure 2 illustrates the experimental results for the first case, TE waveguide modes in a 65 nm thin h-BN flake on SiO_2. Because the mode is launched from the edges of the flake, the h-BN has been patterned in regular shapes to obtain uniform, easier to study interference patterns (Figure 2a–c). The NSOM scans reveal large circular fringes (associated with the focusing of the Gaussian beam on the sample) and, most importantly, a regular set of fringes on the h-BN, indicating the presence of waveguide modes.

The waveguide mode and the incoming beam interfere to form such fringes, which are parallel to the edges confirming their origin from edge scattering (see Supporting Information). Nonguided scattered fields are also observed outside the sample as faint fringes immediately near the edges. Importantly, these fringes are not standing modes on the h-BN flakes. Rather, they originate from the interference of the incident beam with the guided modes launched by each edge and propagating away from it (see Supporting Information for a mathematical description). The absolute position of the fringes depends on the phase relation between the illuminating wave and the launched guided wave at the edge, which is not a trivial problem due to the fringing fields at the edge (an analytical solution exists for polaritons in 2D materials for guided waves reflected at an edge).[35] However, the periodicity of the fringes is not affected by this arbitrary phase factor.

To confirm the exact nature of these modes, FDTD simulations were performed on similar structures (Figure 2d–f). Modeling of h-BN flakes requires careful consideration of the optical anisotropy of the sample, as typical for layered materials, they show different refractive indices for the in-plane ($n_x = n_y$) and out-of-plane (n_z) directions.[24] Using the initial ansatz of $n_x = n_y = n_z = 2.0$ from bulk h-BN, similar fringes are found in the FDTD computed near-field (Figure 2d–f). The FDTD also shows that the guided mode is TE (see Supporting Information, Figure 2), and its presence can be explained by the fact that both air (above) and SiO_2 (below) have smaller refractive indices than h-BN. These conditions lead to the presence of confined TE dielectric waveguide modes. The modes in similar dielectric stacks are well-known, and their TE nature is explained by the fact that TM modes are less confined and in the cutoff region for the h-BN thickness used here.[36] The same is true for higher-order TE modes, resulting in the propagation of first order TE modes alone.

The spatial periodicity of the fringes can be found using a 2D FFT directly on the NSOM images (insets in Figure 2a–c), providing a direct measure of the guided wavelength (Figure 3a) and of the normalized effective index $n_{\mathrm{eff,TE}}$ of the waveguide mode (Figure 3b) as a function of the free space wavelength. Due to TE nature of these modes, their dispersion is independent of the value of n_z, and it depends only on the in-plane refractive index, n_x, and on the thickness of the sample. A series of numerical simulations with different n_x values can be used to obtain the relation $n_{\mathrm{eff,TE}}(n_x)$, given by $\lambda = \lambda_0/n_{\mathrm{eff}}$. Figure 3c shows the extracted n_x of h-BN in the range 550–750 nm. Here, the chosen vdW material, h-BN, is a dielectric with a large bandgap, $E_g \sim 6$ eV; therefore, we assume losses to be negligible in our measurements. The in-plane refractive index

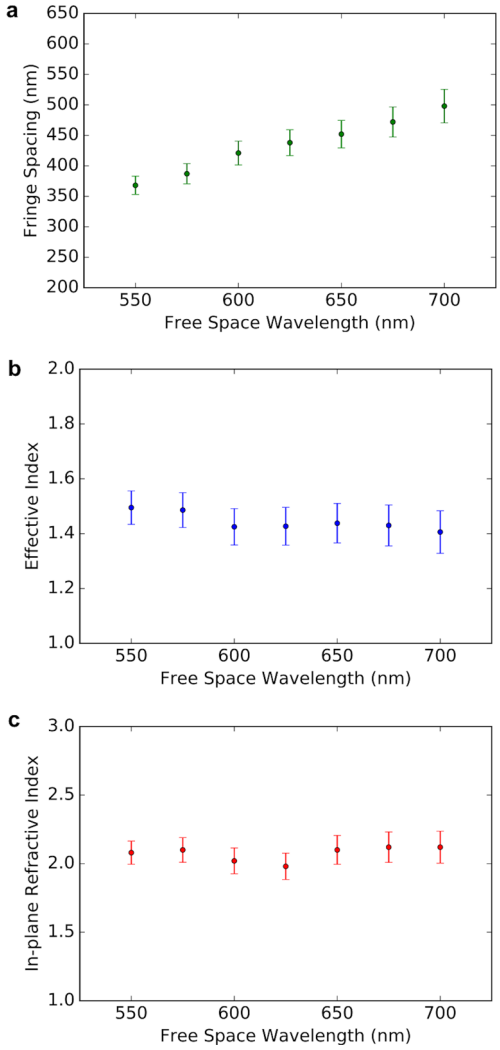

Figure 3. In-plane refractive index measurement. (a) Observed interference fringe spacing as a function of the wavelength. (b) Corresponding effective index of the waveguide mode. (c) Extracted values for the in-plane refractive index of h-BN as a function of wavelength.

over the wavelength range 550–700 nm is in the range 1.98–2.12, corroborating previous studies of the refractive index of h-BN in the visible portion of the spectrum.[24] Observation of interference fringes in both the simulations and NSOM measurements indicates the interference of waveguide modes with the impinging x-axis polarized beam.

The second experiment relies on the use of SPPs, which are TM electromagnetic modes confined at the interface of a metal and a dielectric. They are characterized by an elliptically polarized evanescent electric field and by a well-known dispersion relation dictated by the complex relative electrical permittivities of the dielectric and the metal:

$$k_{\mathrm{SPP}} = k_0\sqrt{\frac{\epsilon_{\mathrm{m}}\epsilon_{\mathrm{d}}}{\epsilon_{\mathrm{m}} + \epsilon_{\mathrm{d}}}} \tag{1}$$

where k_{SPP} is the wavevector of the surface plasmon, k_0 is the free space wavevector, ϵ_{m} is the complex relative electrical permittivity of the metal, and ϵ_{d} is the complex relative electrical permittivity of the dielectric. However, this dispersion relation only holds when the dielectric is isotropic and semi-infinite. For the case of a thin anisotropic dielectric such as h-BN, the dispersion relationship is affected by the anisotropy,

DOI: 10.1021/acsphotonics.7b01518
ACS Photonics 2018, 5, 1196–1201

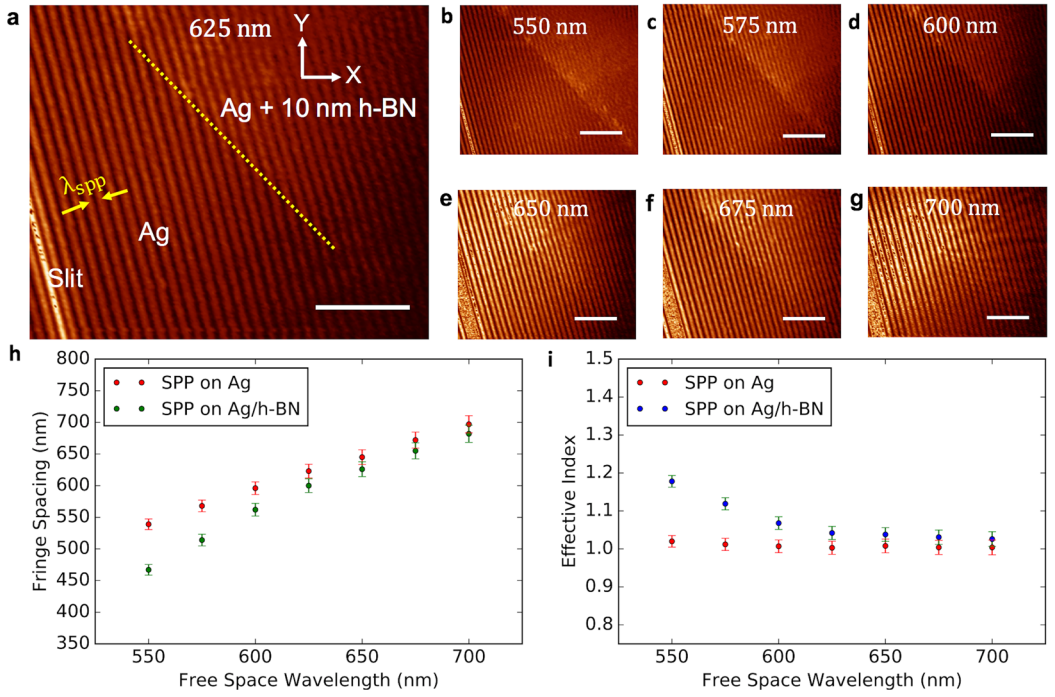

Figure 4. NSOM observation of TM SPP modes in h-BN on Ag. (a–g) NSOM scans for λ_0 in the spectral range 550–700 nm. The slit is positioned in the bottom left corner (not fully pictured) where the optical signal on the detector saturates. The 10 nm h-BN flake is visible from the middle to the right side of the image, as depicted in (a) by a yellow dashed line. (h) Observed SPP interference fringe spacing inside and outside the region covered by the flake. (i) Corresponding SPP effective index, given by $n_{\text{eff}} = \lambda_0/\lambda_{\text{SPP}}$. Scale bars in (a)–(g) are 5 μm.

as the polarization has both in-plane and out-of-plane components (see Figure 1d). Thus, propagation depends on both the in-plane and out-of-plane dielectric constants and can be used to probe them. The dispersion relation of SPPs in the presence of an anisotropic and finite thickness dielectric can be derived as[37]

$$\left(\frac{k_a}{\epsilon_x}+\frac{k_d}{\epsilon_d}\right)\left(\frac{k_a}{\epsilon_x}+\frac{k_m}{\epsilon_m}\right)=\left(\frac{k_a}{\epsilon_x}-\frac{k_d}{\epsilon_d}\right)\left(\frac{k_a}{\epsilon_x}-\frac{k_m}{\epsilon_m}\right)\cdot\exp(-2k_a d) \tag{2}$$

with

$$k_a=\sqrt{\epsilon_x\left(\frac{k_x^2}{\epsilon_z}-\frac{\omega^2}{c^2}\right)},\quad k_d=\sqrt{k_x^2-\epsilon_d\frac{\omega^2}{c^2}},\quad k_m=\sqrt{k_x^2-\epsilon_m\frac{\omega^2}{c^2}} \tag{3}$$

where ϵ_x is the complex relative electrical permittivity of h-BN along x, ϵ_z is the complex relative electrical permittivity of h-BN along z, ϵ_d is the complex relative electrical permittivity of the dielectric superstrate above h-BN which in our case is air (i.e., $\epsilon_d = 1$), ϵ_m is the complex relative electrical permittivity of metal, k_x is the in-plane SPP wavevector, ω is the angular frequency, c is the speed of light, d is the thickness of h-BN, $\epsilon_x = n_x^2$ and $\epsilon_z = n_z^2$. Essentially, a measurement of the effective mode index of the elliptically polarized SPPs in the presence of 10 nm thin anisotropic h-BN, will allow for the extraction of the out-of-plane refractive index, given that the in-plane refractive index is known a priori from the waveguide modes.

Figure 4 summarizes the NSOM experimental results for the near-field SPP experiment. The FIB milled slit is illuminated from the back-side with light polarized perpendicularly to it, launching SPPs with wavefronts parallel to the slit. The initial propagation of the SPPs on the Ag is altered by the presence of the thin film h-BN, which changes the SPP wavelength, λ_{SPP}, due to the different refractive indices. The interference fringes (Figure 4a-g) are spaced by the SPP wavelength, λ_{SPP}. Following the same argument as in the first experiment, an FFT can be used to obtain λ_{SPP} and the corresponding effective index $n_{\text{eff,SPP}}$ (Figure 4h,i). A calibration factor of 1.03 is applied to the data collected at the Ag/h-BN/air interface in an effort to account for the systematic errors before the experimental data are compared to the simulation results (see Supporting Information for detailed description). Strikingly, despite the very low number of h-BN layers, the effect on the SPP propagation is evident, and allows for the extraction of useful information on the sample.

Because the SPP propagation in the presence of the h-BN is affected by both n_x and n_z, this experiment alone is insufficient to extract the value of n_z. However, using the previously measured n_x in the first experiment, n_z can be extracted from FDTD simulations, as outlined in Figure 5a. Figure 5b shows the resulting in-plane and out-of-plane refractive index values of h-BN. Over the wavelength range 550–700 nm, n_z is in the range 1.45–2.12 and n_x is in the range 1.98–2.12.

CONCLUSIONS

2D materials are expected to exhibit new physics when approaching the monolayer limit.[9,13,17−20] However, the ability to experimentally measure the anisotropic refractive indices of a thin, small area material is traditionally a difficult experiment, even for isotropic materials.[38] Our methodology allows us to measure two unknowns-the in-plane and out-of-plane refractive indices of h-BN, which has been used in several works as a dielectric material.[13,21,22] The strategic material choice of h-BN for the proof of principle has two main benefits: previous experiments have shown thin film h-BN to not differ from bulk h-BN too drastically, so the data can be checked against previous experiments and, most importantly, it paves the way for the measurement of materials that require h-BN encapsulation,

DOI: 10.1021/acsphotonics.7b01518
ACS Photonics 2018, 5, 1196−1201

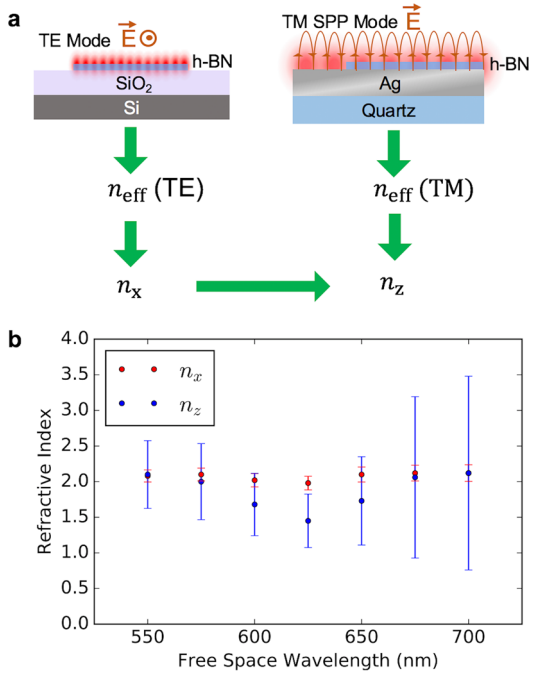

Figure 5. Extraction of anisotropic refractive indices of h-BN. (a) Procedure to extract the anisotropic refractive indices: the in-plane component n_x is first extracted by matching the experimental effective index n_{eff} of the TE mode with the one obtained from numerical FDTD simulation. Thereafter, the out-of-plane n_z component is found from the numerical FDTD simulation by knowing: the thickness from atomic force microscopy measurements and the value of n_x previously extracted from the waveguide mode case and the experimental n_{eff} of the SPP in the presence of h-BN. This procedure is repeated for all wavelengths. (b) Anisotropic refractive indices of h-BN in the spectral range 550−700 nm. Error bars represent the uncertainty due to the limited number of fringes accessible in the NSOM images (see Supporting Information for detailed description of error bar calculation).

such as transition metal dichalcogenides[9,18−20] and black phosphorus.[8,9,15] We anticipate that the knowledge of the optical constants of 2D materials, and particularly the possibility of experimentally accessing their out-of-plane optical properties due to the SPP coupling, will allow for their use in a wider variety of optics experiments and devices.

MATERIALS AND METHODS

Fabrication. *Devices on SiO_2.* h-BN is mechanically exfoliated on to a 285 nm SiO_2/Si substrate with predefined metallic alignment marks. The substrates are then coated with MA-N 2403 (negative electron beam resist) and exposed with an electron beam system with a dose of 1200 $\mu C/cm^2$ using an accelerating voltage of 125 kV. The samples are shaped into rectangles, triangles, or circles. After developing in AZ-726 for 1 min, the samples are postbaked at 100 C for 10 min. Then h-BN is etched by using a reactive ion etching (RIE) system with $CHF_3/Ar/O_2$ at flows of 10/5/2 sccm respectively and a RF generator at 30 W for 2−5 min. After the etching process, exposed MA-N 2403 resist is removed by Remover PG and chloroform. Afterward, the samples are rinsed with isopropyl alcohol (IPA) and dried with nitrogen.

Devices on Ag. A single-crystal 10 nm thin h-BN flake is aligned and transferred to the active device region on the Ag substrate using a standard dry transfer technique.[4]

Numerical Simulations. *Full Wave 3D Simulations.* The Lumerical FDTD 3D wave solver is used to compute the fields in the patterned shapes considered in the experiment. For the case of waveguide modes in 65 nm thick h-BN on top of 285 nm SiO_2/Si, a fine mesh size of 1 nm is used. The monitor is placed 10 nm above the h-BN layer to compute the near-field power of the waveguide mode. A Gaussian source of 650 nm is placed above the geometry.

Effective Indices Simulation and Extraction. The 2D solver Lumerical Mode Solutions is used to compute the mode profile and effective indices for a range of refractive indices of h-BN. For the case of waveguide mode where 65 nm thin h-BN is placed on top of 285 nm SiO_2/Si, h-BN is modeled as an isotropic dielectric, since the propagation is independent of the out-of-plane properties of h-BN. A range of refractive indices for h-BN is swept across to obtain the corresponding effective indices. The refractive index for which the corresponding computed effective index matches that of the experimental effective index measured from NSOM scans, is assigned as the in-plane refractive index of h-BN for that particular wavelength. This process is repeated for other wavelengths. On the other hand, for the case of SPP mode where 10 nm thin h-BN is placed on 50 nm Ag substrate, h-BN is modeled as an anisotropic dielectric and in-plane refractive index from the waveguide mode is used as an input. Thereafter, the out-of-plane refractive index of h-BN is swept across a range to obtain the corresponding effective indices. The out-of-plane refractive index for which the corresponding computed effective index matches that of the experimental effective index measured from NSOM scans, is assigned as the out-of-plane refractive index of h-BN for that particular wavelength. Similarly, this process is repeated for other wavelengths.

ASSOCIATED CONTENT

Supporting Information

The Supporting Information is available free of charge on the ACS Publications website at DOI: 10.1021/acsphotonics.7b01518.

Collection of additional data and methods that supports the main conclusions in the paper (PDF).

AUTHOR INFORMATION

Corresponding Author

*E-mail: capasso@seas.harvard.edu.

ORCID

Kundan Chaudhary: 0000-0003-4253-0942
Antonio Ambrosio: 0000-0002-8519-3862
Michele Tamagnone: 0000-0002-9812-2449
Philip Kim: 0000-0002-8255-0086

Author Contributions

‡These authors contributed equally to this work

Notes

The authors declare no competing financial interest.

ACKNOWLEDGMENTS

This work was supported by the NSF EFRI, Award No. 1542807. This work was performed in part at the Harvard University Center for Nanoscale Systems (CNS), a member of the National Nanotechnology Coordinated Infrastructure Network (NNCI), which is supported by the National Science Foundation under NSF ECCS Award No. 1541959. M.T. acknowledges the support of the Swiss National Science Foundation (SNSF) Grant No. 168545. K.W. and T.T. acknowledge support from the Elemental

DOI: 10.1021/acsphotonics.7b01518
ACS Photonics 2018, 5, 1196−1201

Strategy Initiative conducted by the MEXT, Japan and JSPS KAKENHI Grant No. JP15K217.

REFERENCES

(1) Novoselov, K. S.; Geim, A. K.; Morozov, S. V.; Jiang, D.; Katsnelson, M. I.; et al. Two-dimensional gas of massless Dirac fermions in graphene. *Nature* **2005**, *438*, 197−200.

(2) Zhang, Y.; Tan, Y. W.; Stormer, H. L.; Kim, P. Experimental observation of the quantum Hall effect and Berry's phase in graphene. *Nature* **2005**, *438*, 201−204.

(3) Crossno, J.; Shi, J. K.; Wang, K.; Liu, X.; Harzheim, A.; et al. Observation of the Dirac fluid and the breakdown of the Wiedemann-Franz law in graphene. *Science* **2016**, *351*, 1058−1061.

(4) Wang, L.; Meric, I.; Huang, P. Y.; Gao, Q.; Gao, Y.; et al. One-dimensional electrical contact to a two-dimensional material. *Science* **2013**, *342*, 614−617.

(5) Hunt, B.; Sanchez-Yamagishi, J. D.; Young, A. F.; Yankowitz, M.; LeRoy, B. J.; et al. Massive Dirac fermions and Hofstadter butterfly in a van der Waals heterostructure. *Science* **2013**, *340*, 1427−1430.

(6) Geim, A. K.; Grigorieva, I. V. Van der Waals heterostructures. *Nature* **2013**, *499*, 419−425.

(7) Mas-Balleste, R.; Gomez-Navarro, C.; Gomez-Herrero, J.; Zamora, F. 2D materials: to graphene and beyond. *Nanoscale* **2011**, *3*, 20−30.

(8) Li, L.; Yu, Y.; Ye, G. J.; Ge, Q.; Ou, X.; et al. Black phosphorus field-effect transistors. *Nat. Nanotechnol.* **2014**, *9*, 372−377.

(9) Basov, D.; Fogler, M.; de Abajo, F. G. Polaritons in van der Waals materials. *Science* **2016**, *354*, 1992.

(10) Alonso-Gonzalez, P.; Nikitin, A. Y.; Golmar, F.; Centeno, A.; Pesquera, A.; et al. Controlling graphene plasmons with resonant metal antennas and spatial conductivity patterns. *Science* **2014**, *344*, 1369−1373.

(11) Woessner, A.; Lundeberg, M. B.; Gao, Y.; Principi, A.; Alonso-Gonzalez, P.; et al. Highly confined low-loss plasmons in graphene-boron nitride heterostructures. *Nat. Mater.* **2015**, *14*, 421−425.

(12) Chen, J.; Badioli, M.; Alonso-Gonzalez, P.; Thongrattanasiri, S.; Huth, F.; et al. Optical nano-imaging of gate-tunable graphene plasmons. *Nature* **2012**, *487*, 77−81.

(13) Dai, S.; Fei, Z.; Ma, Q.; Rodin, A. S.; Wagner, M.; et al. Tunable phonon polaritons in atomically thin van der Waals crystals of boron nitride. *Science* **2014**, *343*, 1125−1129.

(14) Yao, Y.; Kats, M. A.; Genevet, P.; Yu, N.; Song, Y.; et al. Broad electrical tuning of graphene-loaded plasmonic antennas. *Nano Lett.* **2013**, *13*, 1257−1264.

(15) Engel, M.; Steiner, M.; Avouris, P. Black phosphorus photodetector for multispectral, high-resolution imaging. *Nano Lett.* **2014**, *14*, 6414−6417.

(16) Gan, X.; Shiue, R. J.; Gao, Y.; Meric, I.; Heinz, T. F.; et al. Chip-integrated ultrafast graphene photodetector with high responsivity. *Nat. Photonics* **2013**, *7*, 883−887.

(17) Britnell, L.; Ribeiro, R. M.; Eckmann, A.; Jalil, R.; Belle, B. D.; et al. Strong light-matter interactions in heterostructures of atomically thin films. *Science* **2013**, *340*, 1311−1314.

(18) Shi, H.; Yan, R.; Bertolazzi, S.; Brivio, J.; Gao, B.; et al. Exciton dynamics in suspended monolayer and few-layer MoS_2 2D crystals. *ACS Nano* **2013**, *7*, 1072−1080.

(19) Chernikov, A.; Berkelbach, T. C.; Hill, H. M.; Rigosi, A.; Yilei, L.; et al. Exciton binding energy and nonhydrogenic Rydberg series in monolayer WS_2. *Phys. Rev. Lett.* **2014**, *113*, 076802.

(20) Qiu, D. Y.; Felipe, H.; Louie, S. G. Optical spectrum of MoS_2: many-body effects and diversity of exciton states. *Phys. Rev. Lett.* **2013**, *111*, 216805.

(21) Watanabe, K.; Taniguchi, T.; Kanda, H. Direct-bandgap properties and evidence for ultraviolet lasing of hexagonal boron nitride single crystal. *Nat. Mater.* **2004**, *3*, 404−409.

(22) Caldwell, J. D.; Kretinin, A. V.; Chen, Y.; Giannini, V.; Fogler, M. M.; et al. Sub-diffractional volume-confined polaritons in the natural hyperbolic material hexagonal boron nitride. *Nat. Commun.* **2014**, *5*, 5221.

(23) Low, T.; Chaves, A.; Caldwell, J. D.; Kumar, A.; Fang, N. X.; et al. Polaritons in layered two-dimensional materials. *Nat. Mater.* **2017**, *16*, 182−194.

(24) Schubert, M.; Rheinlander, B.; Franke, E.; Neumann, H.; Hahn, J.; et al. Anisotropy of boron nitride thin-film reflectivity spectra by generalized ellipsometry. *Appl. Phys. Lett.* **1997**, *70*, 1819−1821.

(25) Ambrosio, A.; Allegrini, M.; Latini, G.; Cacialli, F. Thermal processes in metal-coated fiber probes for near-field experiments. *Appl. Phys. Lett.* **2005**, *87*, 033109.

(26) Ambrosio, A.; Camposeo, A.; Maddalena, P.; Patanè, S.; Allegrini, M. Real-time monitoring of the surface relief formation on azo-polymer films upon near-field excitation. *J. Microsc.* **2008**, *229*, 307−312.

(27) Horcas, I.; Fernandez, R.; Gomez-Rodriguez, J. M.; Colchero, J.; et al. WSXM: a software for scanning probe microscopy and a tool for nanotechnology. *Rev. Sci. Instrum.* **2007**, *78*, 013705.

(28) Ambrosio, A.; Cefali, E.; Spadaro, S.; Patane, S.; et al. Noncontact tuning fork position sensing for hollow-pyramid near-field cantilevered probes. *Appl. Phys. Lett.* **2006**, *89*, 163108.

(29) Liu, W.; Lee, B.; Naylor, C. H.; Ee, H. S.; Park, J.; et al. Strong exciton-plasmon coupling in MoS_2 coupled with plasmonic lattice. *Nano Lett.* **2016**, *16*, 1262−1269.

(30) Grigorenko, A. N.; Polini, M.; Novoselov, K. S. Graphene Plasmonics. *Nat. Photonics* **2012**, *6*, 749−758.

(31) Xia, F.; Wang, H.; Xiao, D.; Dubey, M.; Ramasubramaniam, A. Two-dimensional material nanophotonics. *Nat. Photonics* **2014**, *8*, 899−907.

(32) Wintz, D.; Genevet, P.; Ambrosio, A.; Woolf, A.; Capasso, F. Holographic metalens for switchable focusing of surface plasmons. *Nano Lett.* **2015**, *15*, 3585−3589.

(33) Genevet, P.; Wintz, D.; Ambrosio, A.; She, A.; Blanchard, R.; et al. Controlled steering of Cherenkov surface plasmon wakes with a one-dimensional metamaterial. *Nat. Nanotechnol.* **2015**, *10*, 804−809.

(34) Huber, A. J.; Ocelic, N.; Hillenbrand, R. Local excitation and interference of surface phonon polaritons studied by near-field infrared microscopy. *J. Microsc.* **2008**, *229*, 389−395.

(35) Nikitin, A. Yu.; Low, T.; Martin-Moreno, L. Anomalous reflection of graphene plasmons and its influence on resonators. *Phys. Rev. B: Condens. Matter Mater. Phys.* **2014**, *90*, 041407.

(36) Saleh, B. E. A.; Teich, M. C. *Fundamentals of Photonics*; Wiley: New York, 1991.

(37) Li, X.; Gu, Y.; Luo, R.; Wang, L.; Gong, Q. Effects of dielectric anisotropy on surface plasmon polaritons in three-layer plasmonic nanostructures. *Plasmonics* **2013**, *8*, 1043−1049.

(38) Govyadinov, A. A.; Mastel, S.; Golmar, F.; Chuvilin, A.; Carney, P. S.; Hillenbrand, R. Recovery of permittivity and depth from near-field data as a step toward infrared nanotomography. *ACS Nano* **2014**, *8* (7), 6911−6921.

NOTE ADDED AFTER ASAP PUBLICATION

This paper was published ASAP on February 2, 2018, with an error in panel b of Figure 2. The corrected version was reposted on February 7, 2018.

DOI: 10.1021/acsphotonics.7b01518
ACS Photonics 2018, 5, 1196−1201